Recapitulation of Unilateral Cleft Lip Nasal Deformity on Normal Nasal Structure: A Finite Element Model Analysis

Article *in* Journal of Craniofacial Surgery · October 2018

DOI: 10.1097/SCS.0000000000005024

CITATIONS
3

READS
101

7 authors, including:

Hanyao Huang
Sichuan University
19 PUBLICATIONS **22** CITATIONS
SEE PROFILE

Xiangyou Luo
University of California, Los Angeles
17 PUBLICATIONS **82** CITATIONS
SEE PROFILE

Jingtao Li
National University of Singapore
41 PUBLICATIONS **132** CITATIONS
SEE PROFILE

Recapitulation of Unilateral Cleft Lip Nasal Deformity on Normal Nasal Structure: A Finite Element Model Analysis

Hanyao Huang, MD, Xiangyou Luo, MD,* Xu Cheng, MD,* Zihao Zhang, BA,† Guanqiu Ma, BA,‡ Bing Shi, MD, PhD,* and Jingtao Li, MD, PhD**

Abstract: Cleft lip nasal deformity has been challenging to plastic surgeons. A better understanding of the biomechanical aspect of the cleft nose would contribute to a better correction. In this study, finite element model of a normal nose was constructed and loaded with forces to recapitulate the unilateral cleft lip nasal deformity. Tether at the alar base was simulated by a laterally directed force at the lateral crus, and tether at the columella base by a posteriorly directed force at the medial crus. The equivalent von-Mises stress and the total deformation consequent to different patterns of loading were captured. In accordance with clinical observations, unilaterally loaded forces caused deformation on both sides of the nose. A correlation between the patterns of loading and different cleft lip nasal deformities was documented in detail. When set at the same force magnitude, tether at the columella base led to more extensive changes in the nasal morphology and higher level of stress than at the alar base. Clear identification of major pathological tethers in the nasolabial region might lead to more accurate and stable correction of cleft lip nasal deformities.

Key Words: 3D modeling, cleft lip, finite element analysis, nasal deformity, pathological tether

(*J Craniofac Surg* 2018;29: 2220–2225)

Cleft lip and palate deformity is one of the most common congenital anomalies in human, with its occurrence varying among races.[1,2] Besides its functional consequences including impeded speech, feeding, and hearing, the major impact of cleft lip deformity is from the disfigurement in the central region of the face. When cleft lip occurs, both the tissue continuity and the muscular force balance in the nasolabial region become interrupted, with the nose distorted into a collapsed and asymmetrical shape. Although the lip could usually be restored decently, the nasal deformity persists in most cleft cases even after multiple corrections. Actually, nasal deformity has become the most notable stigma inflicted by cleft lip and the top concern in modern cleft management.[3]

The obstacle to a better correction outcome lies in our limited understanding of the developmental mechanism of unilateral cleft lip nasal deformity. The contour of the nose is decided by its underlying cartilage framework. The alar cartilage, which dictates the projection of the nasal tip and the shape of the alar dome, suffers from both hypoplasia and displacement among cleft patients. Such displacement and hypoplasia of the alar cartilage are demonstrated as pathological tethers. Pathological tethers on the lateral crus as well as the medial crus are regarded as the begin alteration factor that distorts the nose over time. Adequate release of pathological tethers has been recognized as the key to a successful correction of cleft nasal deformities, but the detailed correlations between each pathological tether and specific deformity characteristics are largely unknown. A better understanding of the influence of static and dynamic forces generated by pathological tethers on the nasal structure is critical to the improvement of cleft lip rhinoplasty,[4] and biomechanics research tools are providing potential opportunities to further our understandings.

With the wide application of computational technology, including digital simulation, computer aided design/computer aided manufacturing (CAD/CAM), and computer-assisted surgery, the significance of biomechanics has manifested clearly. For an example, the evaluation of implant supported prosthesis could help to achieve a better restorative prognosis.[5–11] For the past decade, finite element modeling has also been validated as a helpful biomechanic tool in the study of rhinoplasty. By dividing the complex structure of nose into a collection of subdomains, finite element analysis (FEA) can efficiently identify regions with high levels of distortion or stress. For example, FEA has been successfully applied in the studies of the formation of the inverted-V deformity,[4] the effectiveness of the septal L-strut,[12,13] and the form of the nasal tip.[14–17] In the field of cleft lip and palate, FEA has been employed in analyzing the maxillary bone.[18–20] Its advantage, however, has rarely been taken in the study of cleft lip nasal deformity.[21] Unlike normal nose or aesthetic rhinoplasty, the unilateral cleft lip nasal deformity was characterized by asymmetry and severe tissue displacement, which have rarely been taken into consideration in previous studies. Moreover, the nasal structure in previous studies was constructed arbitrarily based on subjective experience in nasal anatomy, which would sacrifice the accuracy of the model.

In this study, a finite element model was constructed based on the magnetic resonance imaging (MRI) of a normal nose and loaded with forces recapitulating pathological tethers on the nasal

From the *State Key Laboratory of Oral Diseases, National Clinical Research Center for Oral Diseases, Department of Oral Maxillofacial Surgery, West China Hospital of Stomatology, Sichuan University, Chengdu; †Institute of Computing Technology, University of Chinese Academy of Sciences, Beijing; and ‡Beijing Computational Science Research Center, Beijing, China.

Received February 14, 2018.

Accepted for publication August 8, 2018.

Address correspondence and reprint requests to Jingtao Li, MD, PhD, West China Hospital of Stomatology, Chengdu, Sichuan, China; E-mail: lijingtao86@163.com

This work was supported by the Sichuan Science and Technology Program grant to JL (2017RZ0036).

The authors report no conflicts of interest.

Supplemental digital contents are available for this article. Direct URL citations appear in the printed text and are provided in the HTML and PDF versions of this article on the journal's Web site (www.jcraniofacialsurgery.com).

ISSN: 1049-2275

DOI: 10.1097/SCS.0000000000005024

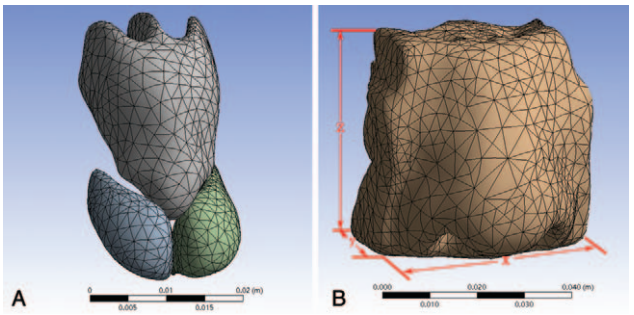

FIGURE 1. The CAD model for FEA. (A) Isolated nasal cartilage framework (alar cartilage in green and blue, T-bar complex in grey). (B) Cartilage framework covered by overlying skin envelope. FEA, finite element analysis.

structure. The consequent morphological distortion and stress distribution were analyzed. By recapitulating the cleft lip nose characteristics on a normal nose structure, we set out to establish correlative relationships between pathological tethers and specific deformity characteristics.

MATERIALS AND METHODS

Magnetic Resonance Imaging

A healthy 23-year-old Chinese Han female volunteer was enrolled in November, 2016. Clinical examination revealed no notable deviation or asymmetry in the outer nose of the volunteer. Magnetic resonance imaging scanning (repetition time/echo time, 1900/2.94; voxel size, $1.0 \times 1.0 \times 1.0$ mm; field of view, 250×250 mm; matrix, 245×256; slice thickness, 1.00 mm; and sections per slab, 176) covering the nasal region was performed in the Department of Radiology, West China Hospital of Sichuan University. DICOM-format images were exported into Mimics 15.0 (Mimics, Materialise, Leuven, Belgium) for reconstruction.

Nasal Model Construction

The nasal model was constructed according to the MRI data. The cartilage framework consisted of two alar cartilages and a T-bar-shaped cartilaginous complex including the septal cartilage and the upper lateral cartilages (Fig. 1). The cartilage framework and the skin envelope were assembled in Pro/Engineer 5.0 (Pro/E) (PTC, Needham, MA). The dimensions of each cartilage component were presented in Table 1. Physical properties of the cartilages and the skin envelope were assigned according to published data, as presented in Table 2.[4] Finally, mesh generation of the model was performed in Workbench 15.0 (ANSYS Inc., Canonsburg, PA) and exported in ASM format.[22] The definition details of the meshwork were presented in Table 3.

Finite Element Simulation

The lateral margin of the skin envelope and the cranial margin of the cartilage framework were set as fixed for recapitulate perpendicular fibrous bundles anchoring the outer nose to its underlying skeleton. The interactions between the cartilages and skin envelope were set as bonded to simulate the total contact surface between the soft tissue and cartilage. The model was loaded with forces of different vectors on the left side to simulate pathological tether observed in cleft lip nasal deformity. Tether at the alar base was mimicked by laterally directed force loaded at the lateral crus, while tether at the columella base was mimicked by posteriorly directed force loaded at the medial crus (Fig. 2). The value of each force was set at 5 N, which was decided through a trial-and-error process in preliminary simulations. Simulations required intensive use of the computer processor, with each taking about 15 minutes.[10] Static structural analysis was performed to calculate the equivalent von-Mises stress (EQV) and the total deformation (TD).

The research protocol was censored and approved by the Ethics Committee of West China Hospital of Stomatology, Sichuan University (Approval No. WCHSIRB-D-2016-084R1). Individual participants could not be identified during or after data collection.

TABLE 1. Dimensional Definition of the Finite Element Model

Geometry	Length X (x; mm)	Length Y (y; mm)	Length Z (z; mm)	Volume (v; mm^3)
Skin envelope	47.93	62.42	47.96	68,920.55
Alar cartilage	8.86	13.83	15.05	430.34
T-bar-shaped cartilaginous complex	17.98	24.62	25.51	2644.36

TABLE 2. Elastic Properties of Materials for the Finite Element Model

Components[4]	Young's Modulus (MPa)	Density (kg/m^3)	Poisson Ratio
Skin envelope	0.5	980	0.33
Nasal cartilage	0.8	1080	0.15

TABLE 3. Definition of Finite Element Model in ANSYS Workbench.

Geometry	Skin Envelope	Left Alar Cartilage	Right Alar Cartilage	T-Bar-Shaped Cartilaginous Complex	Total
Nodes	38,453	3360	2735	5815	50,363
Elements	23,158	1805	1451	3140	29,554

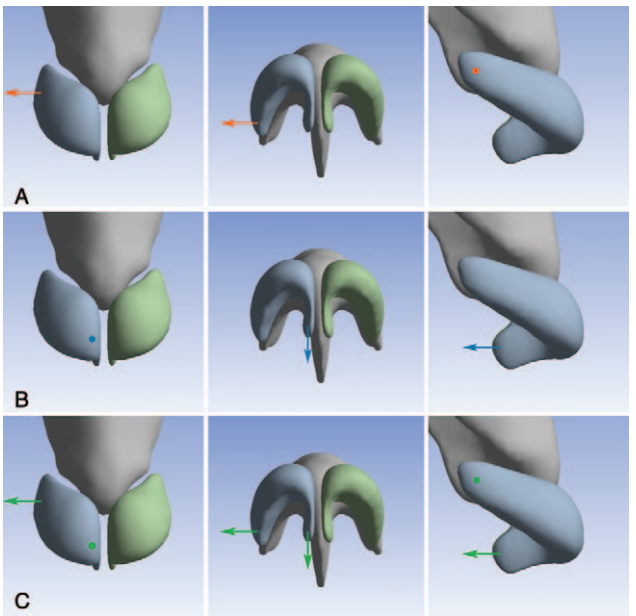

FIGURE 2. Directions of forces for CAD model. (A) Direction of the force at the right lateral crus (orange arrow). From left to right, frontal view, basal view, and lateral view. (B) Direction of the force at the medial crus (blue arrow). (C) The two forces loaded at the same time (green arrow).

RESULTS

Deformation of the model was scaled in millimeter with the direction demonstrated in color-coded arrows. Stress distribution was evaluated by EQV, which was a scalar value that combined the normal and shear stresses for each element under a complex three-dimensional (3D) loading condition.[23]

When the model was first loaded with a laterally directed force mimicking the tether at the lateral crus on the cartilage framework, the EQV concentrated around the loaded lateral crus, its neighboring region on the ipsilateral upper lateral cartilage, and the contralateral alar cartilage (Fig. 3A-C). The maximum deformation on the cartilage framework was observed at the tip of the loaded lateral crus, extending all the way to the ipsilateral intermediate crus, the medial crus, the upper lateral cartilage, and the contralateral alar cartilage, with gradual attenuation (Fig. 3D-F). On the skin envelope, similar to the cartilage framework, the maximum deformation was observed at the dome, affecting the nasal tip, the ipsilateral alar base, the columella, and extending to the contralateral alar dome (Fig. 3G-I). The overall deformation was laterally directed in accordance with the force loaded. The real-time simulation of this loading process was demonstrated in Figure E1 (see Figure, Supplemental Digital Content 1, http://links.lww.com/SCS/A380).

When the model was loaded with posteriorly directed force mimicking the tether at the medial crus, the EQV concentrated around the loaded medial crus, its neighboring region on the contralateral medial crus, and the neighboring upper cartilage (Fig. 4A-C). The maximum deformation was observed at the tip of the loaded medial crus, affecting the entire ipsilateral alar cartilage and the contralateral alar cartilage (Fig. 4D-F). On the skin envelope, the maximum deformation was observed at the nasal tip, extending roughly symmetrically at both sides with gradual attenuation (Fig. 4G-I). The overall deformation was posteriorly directed. The real-time simulation of this loading process was demonstrated in Figure E2 (see Figure, Supplemental Digital Content 2, http://links.lww.com/SCS/A381).

When the model was loaded with both forces, the EQV concentrated around the loaded alar cartilage all the way from the lateral crus to the medial crus (Fig. 5A-C). The deformation reached maximum at the loaded medial crus and the ipsilateral lateral crus, and extended all the way to the entire cartilage framework on the other side (Fig. 5D-F). The maximum deformation on the skin envelope was observed at the nasal tip, extending to neighboring region including the alar and the columella on both sides with gradual attenuation (Fig. 5G-I). The real-time simulation of this loading process was demonstrated in Figure E3 (see Figure, Supplemental Digital Content 3, http://links.lww.com/SCS/A382).

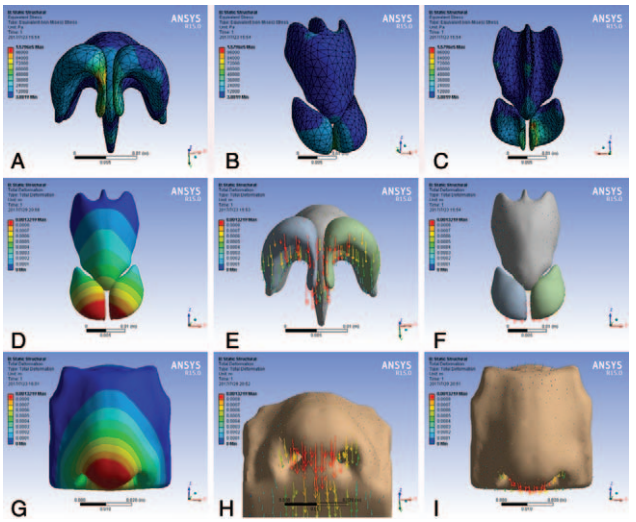

FIGURE 4. Stress and deformation consequent to posteriorly directed force loaded at the medial crus. (A-C) Equivalent von-Mises stress on the nasal framework. The magnitude of the stress was color-coded, as the red indicating the maximum whereas the blue indicating the minimal. (D-F) Total deformation on the nasal framework and (G-I) the skin envelope. The extent of deformation was color-coded, with the red representing the maximum deformation while the blue representing the minimal. The arrow indicated the direction of the deformation.

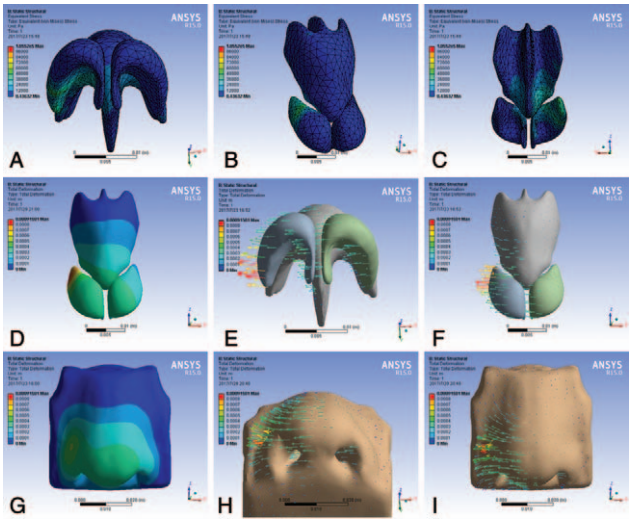

FIGURE 3. Stress and deformation consequent to laterally directed force loaded at the lateral crus. (A-C) Equivalent von-Mises stress on the nasal framework. The magnitude of the stress was color-coded, as the red indicating the maximum whereas the blue indicating the minimal. (D-F) Total deformation on the nasal framework and (G-I) the skin envelope. The extent of deformation was color-coded, with the red representing the maximum deformation while the blue representing the minimal. The arrow indicated the direction of the deformation.

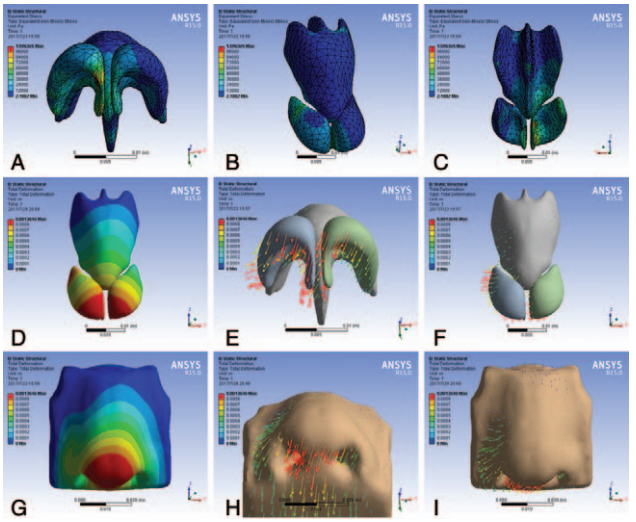

FIGURE 5. Stress and deformation consequent to both forces loaded at the same time. (A-C) Equivalent von-Mises stress on the nasal framework. The magnitude of the stress was color-coded, as the red indicating the maximum whereas the blue indicating the minimal. (D-F) Total deformation on the nasal framework and (G-I) the skin envelope. The extent of deformation was color-coded, with the red representing the maximum deformation while the blue representing the minimal. The arrow indicated the direction of the deformation.

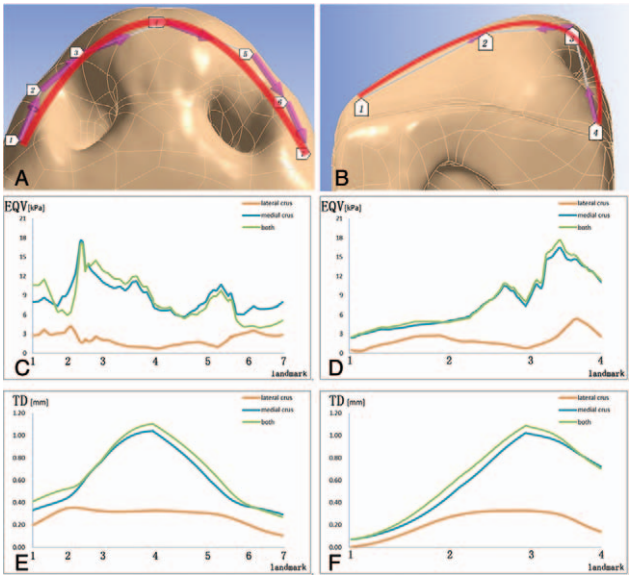

FIGURE 6. Equivalent von-Mises stress and TD on two paths on the skin envelope. (A) Path one was defined by seven landmarks: bilateral alar bases, bilateral nasal domes, the midpoints between the alar base and the nasal dome, and the nasal tip. (B) Path two was defined by four landmarks: the columella base, the nasal tip, the dorsum, and the nasal radix. (C) Equivalent von-Mises stress on Path one. (D) Equivalent von-Mises stress on Path two. (E) Total deformation on Path one. (F) Total deformation on Path two. TD, total deformation.

Two paths were defined on the skin surface to specify the EQV and TD at critical nasal landmarks. Path one was defined by the alar bases at both sides (Landmarks one, seven), the alar domes at both sides (Landmarks three, five), the midpoints between the domes and the alar bases (Landmarks two, six) and the nasal tip (Landmark four) (Fig. 6A). Path two was defined by the nasal radix (Landmark one), the dorsum (Landmark two), the nasal tip (Landmark three), and the columella base (Landmark four) (Fig. 6B). When set at the same magnitude, the force loaded at the lateral crus generated significantly lower EQV and smaller TD than the force at the medial crus. When the lateral crus was loaded, EQV was evenly distributed with a slight increase near the alar domes (Fig. 6C Orange), the nasal dorsum, and the columella (Fig. 6D Orange). When the medial crus was loaded, the maximum stress was observed at the alar domes (Fig. 6C Blue) and the columella (Fig. 6D Blue). When the lateral crus was loaded, the TD was evenly distributed among landmarks on Path one (Fig. 6E Orange), but concentrated around the nasal tip on Path two (Fig. 6F Orange). When the medial crus was loaded, the TD concentrated around the nasal tip both on Path one and two (Fig. 6E-F Blue). When the model was loaded with two forces at the same time, the results were similar to loading force on the medial crus alone (Fig. 6C-F Green).

DISCUSSION

Surgeons have long been studying the nose by modeling its structure. Early in 1998, Fisher and Mann designed a 3D paper model to analyze the alar cartilage structure of cleft lip nose,[24] which was based purely on subjective experience. With the advances in imaging technology and the aid of the FEA, it becomes possible to model both the cartilage framework and the skin envelope of the nose with higher accuracy, and to simulate the deformation and the stress distribution with supreme sensitivity.

For the past decade, FEA has been successfully applied in the biomechanical analyses of rhinoplasty, covering the nasal septum,[12,13,25–28] the alar cartilages,[29] the inverted-V deformity after surgery,[4] the nasal tip,[14–17] the nasal implants,[30] and the nasal airflow.[31–36] Our recent work revealed the functions of specific surgical maneuvers in secondary cleft nose correction.[21] The advantages of FEA are obvious: first, we can specify the exact deformation and stress within the model; second, the cost of it is extremely low. Different from previous researches,[4,13,15] MRI scanning data was used here for modeling. The nasal cartilage could not be differentiated in the computed tomography scanning data but could be clearly visualized in the MRI. Consequently, the dimension and position of the alar cartilages in our modeling was of superior accuracy.

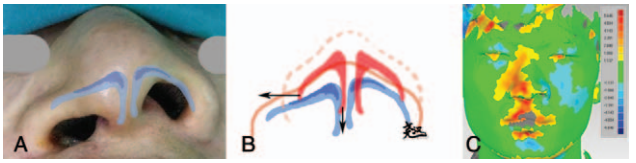

FIGURE 7. Sketch for secondary unilateral cleft lip nasal deformity. (A) A typical unilateral cleft lip nasal deformity, with the shape of the alar cartilages, marked out. (B) Illustration of the cartilage displacement in our modeling. (C) Morphological changes before and after surgical correction of cleft lip nasal deformity. The extent of the deformation was indicated in the color-coded scale bar.

The formation mechanism of cleft lip nose was attributed to the anatomical displacement and hypoplasia of the alar cartilage. The major features of a typical unilateral cleft lip nasal deformity are as follows:

1. downward displacement of the alar cartilage at the cleft side;
2. buckling of the lateral crus at the cleft side; and
3. deviation of the columella base to the noncleft side.[37]

During the surgical correction of such deformities, major tethers were detected in two regions, the dome and the nasal tip (Fig. 7A-B). By loading the normal nasal structure with forces mimicking these tethers, we successfully recapitulated the unilateral cleft lip nasal deformity in a normal nose model. Two forces were chosen, a laterally directed force loaded on the lateral crus mimicking the tether at the alar base and a posteriorly directed force loaded on the medial crus mimicking the tether at the columella base.

Different tethers lead to different patterns of deformation. Force on the lateral crus led to lateral displacement of the alar base, resulting in horizontal rotation of the nostril at the cleft side. Force on the medial crus, however, mainly led to downward displacement of the nasal tip. Nevertheless, it was also observed that the force at the lateral crus could affect the nasal tip, as well as the force at the medial crus could affect the dome and even the alar base.

Tether at the medial crus leads to greater level of stress and deformation. When set at the same magnitude, the force on the medial crus led to significantly higher level of stress and deformation than the force on the lateral crus (Fig. 6). When the two forces were loaded at the same time, the results were almost the same as when the force on the medial crus was loaded alone, suggesting that the tether at the medial crus was easier to detect. One possible explanation was that the medial crus was on the midline and could influence both sides more easily than the lateral crus. It might be consequently deduced that, during cleft lip nasal deformity correction, release at the columella base might be more critical to the outcome.

Unilateral tether influences both sides of the nose. As our results indicated, each force could extend its effect to the contralateral side. Deformation and stress concentration were observed not only at the force loading spot, but also the neighboring and contralateral regions, which was consistent with general clinical experience.

Within the architecture of nose, localized tether would lead to a chain reaction of morphology changes, and no part can stay unaffected.

This study also suggested that different types of cleft lip nasal deformities might be of varied causes. Medial tether could be released by columella lengthening with tissues from upper lip or nasal sill, while lateral tether could be released by dome V–Y plasty. It might further suggest that existing pathological tethers should be clarified before determining the surgical plan for cleft lip nasal deformity correction. Unlike deformities caused by injuries that are of disparate demonstrations, cleft lip deformities are of characteristic features. Some generalized surgical techniques, for example, the most widely used rotation-advancement technique, can be applied to most cleft lip cases with satisfactory outcomes. Similarly, the association between the tethers and the patterns of deformation and stress, we generalized, are of predictive value to most cleft lip noses. For example, in a patient-specific circumstance, the severity of the deformity at the nasal tip or at the alar base suggests that pathological tether should be given the most attention during the correction. For clinical validation, we acquired the nasal morphology of a patient with unilateral cleft lip nasal deformity both before and after the surgery, using 3D photography (3dMDface system, Atlanta, GA). The pre- and postoperative 3D photos were overlapped to visualize the changes in morphology (Fig. 7C). The color-coded changes were very close to the deformation pattern generated by the simultaneous force loading at the medial and lateral crura (Fig. 5).

We chose a normal nasal structure instead of a cleft one for analyses. The purpose of this study was to identify the major tethers that need to be released during cleft nose correction, in another word, the tethers that pull a normal nasal framework into a cleft nose in the utero, which is a ''dynamic'' process. Once a cleft nose is formed, the tethers become ''quiescent'' and a pathological stress-free equilibrium was achieved. If the finite element model was constructed based on a cleft nose MRI, we could only test stress pattern caused by the corrective forces instead of the pathological tethers. Meanwhile, the resolution of present MRI is not sufficient for distinguishing the infant cartilages because the development of the cartilages is not completed yet. As a result, we chose to construct the model in a reverse way, where the morphology of a normal nose was used as the original template. Since we demonstrated the correlation between the abnormal morphology and potential major tethers in cleft lip nasal deformity, plastic surgeons might be able to choose a more appropriate and specific maneuver when performing the corrective procedure. For example, considering releasing tether at the medial crus around the columella to correct a severe tip collapse, or focusing on tether release at lateral crus when restoring a flat discontinued nasal sill. These perspectives should always be comprehensively applied during clinical decision-making and practice.

In order to mimic the ''dynamic'' process of the stress pattern formation, real-time simulations with a duration of 5 seconds were performed for each loading circumstances (see Supplemental Digital Content, Figures E1–E3, http://links.lww.com/SCS/A380, http://links.lww.com/SCS/A381, and http://links.lww.com/SCS/A382). The endpoint stress distribution was the same as our previous description, and the stress generally extended from the force-loading point, either lateral crus or medial crus, towards the nasal tip as the time went.

This study bore the intrinsic limitations shared by all theoretical models. First of all, the properties of human tissue are not homogeneous, which would definitely influence the mechanical results. Unlike the highly mobile tissue on the cheek or lip, the soft tissue covering the nasal cartilage framework is of tight skin with a very thin layer of subcutaneous tissue. When the nose was modeled with viscoelastic–hyperelastic constitutive equations, the morphology deformation was far beyond the range of clinical observation, which might explain why all previous computational simulations of nasal structures, especially the skin envelope, were modeled with linear material properties.[4,15,16]

In addition, the exact values of the tethering forces were not available, and 5 N was chosen through a trial-and-error process in preliminary simulations, where the generated deformation on the skin envelope was mostly close to the reality. Moreover, the loading spot and direction of the force were chosen based on experience.

The peripheral nodes of the model were set as fixed for two major reasons. First, when loaded with exogenous forces, displacement in the skin envelope at the margin of the outer nose is minor. Numerous perpendicular fibrous bundles anchored the outer nose to its underlying skeleton, so as to maintain the position of the nose relative to the face.[37] Second, since the force loaded on the model was of no counterparts exerted at a reverse direction, the model would demonstrate significant drifting if the lateral margin was not set fixed.

To manage the cleft lip nasal deformity properly, we believe a surgeon should go through three stages. Stage one is to understand how the deformity happens, including the pathology and mechanism of the deformity. Stage two is to concentrate on how to fix the existing deformation to a normal status. Stage three is about the relapse, which is a huge challenge to cleft surgeons. If a cleft surgeon does not remove the existed pathological factors during correction, such as releasing the pathological tethers, or chooses unsuitable surgical maneuvers to do so, the relapse would be inevitable. The objectives of our study were generated by reverse thinking the stage one problem. Unilateral cleft lip nasal deformity was successfully recapitulated in a finite element model of a normal nose in this study. Forces mimicking pathological tethers generated different patterns of deformation and stress distribution. Concrete identification of major pathological tethers in the nasolabial region might lead to more accurate surgical planning and more stable correction outcomes.

REFERENCES

1. Vyas RM, Warren SM. Unilateral cleft lip repair. *Clin Plast Surg* 2014;41:165–177
2. Tse R. Unilateral cleft lip: principles and practice of surgical management. *Semin Plast Surg* 2012;26:145–155
3. He X, Shi B, Kamdar M, et al. Development of a method for rating nasal appearance after cleft lip repair. *J Plast Reconstr Aesthet Surg* 2009;62:1437–1441
4. Tjoa T, Manuel CT, Leary RP, et al. A finite element model to simulate formation of the inverted-V deformity. *JAMA Facial Plast Surg* 2016;18:136–143
5. Lauritano F, Runci M, Cervino G, et al. Three-dimensional evaluation of different prosthesis retention systems using finite element analysis and the Von Mises stress test. *Minerva Stomatol* 2016;65:353–367
6. Cicciu M, Risitano G, Maiorana C, et al. Parametric analysis of the strength in the "Toronto" osseous-prosthesis system. *Minerva Stomatol* 2009;58:9–23
7. Cicciù M, Cervino G, Bramanti E, et al. FEM analysis of mandibular prosthetic overdenture supported by dental implants: evaluation of different retention methods. *Comput Math Methods Med* 2015;2015:943839
8. Cicciu M, Bramanti E, Matacena G, et al. FEM evaluation of cemented-retained versus screw-retained dental implant single-tooth crown prosthesis. *Int J Clin Exp Med* 2014;7:817–825
9. Cicciù M, Bramanti E, Cecchetti F, et al. FEM and Von Mises analyses of different dental implant shapes for masticatory loading distribution. *Oral Implantol (Rome)* 2014;7:1–10
10. Cervino G, Romeo U, Lauritano F, et al. Fem and Von Mises analysis of OSSTEM® dental implant structural components: evaluation of different direction dynamic loads. *Open Dent J* 2018;12:219–229

11. Bramanti E, Cervino G, Lauritano F, et al. FEM and Von Mises analysis on prosthetic crowns structural elements: evaluation of different applied materials. *Sci World J* 2017;2017:1029574
12. Lee JS, Lee DC, Ha DH, et al. Redefining the septal L-strut to prevent collapse. *PLoS One* 2016;11:e0153056
13. Lee JS, Lee DC, Ha DH, et al. Redefining the septal L-strut in septal surgery. *PLoS One* 2015;10:e0119996
14. Manuel CT, Harb R, Badran A, et al. Finite element model and validation of nasal tip deformation. *Ann Biomed Eng* 2017;45:829–838
15. Shamouelian D, Leary RP, Manuel CT, et al. Rethinking nasal tip support: a finite element analysis. *Laryngoscope* 2015;125:326–330
16. Leary RP, Manuel CT, Shamouelian D, et al. Finite element model analysis of cephalic trim on nasal tip stability. *JAMA Facial Plast Surg* 2015;17:413–420
17. Manuel CT, Leary R, Protsenko DE, et al. Nasal tip support: a finite element analysis of the role of the caudal septum during tip depression. *Laryngoscope* 2014;124:649–654
18. Olmez S, Dogan S, Pekedis M, et al. Biomechanical evaluation of sagittal maxillary internal distraction osteogenesis in unilateral cleft lip and palate patient and noncleft patients: a three-dimensional finite element analysis. *Angle Orthod* 2014;84:815–824
19. Pan X, Qian Y, Yu J, et al. Biomechanical effects of rapid palatal expansion on the craniofacial skeleton with cleft palate: a three-dimensional finite element analysis. *Cleft Palate Craniofac J* 2007;44:149–154
20. Nagasao T, Miyamoto J, Konno E, et al. Dynamic analysis of the effects of upper lip pressure on the asymmetry of the facial skeleton in patients with unilateral complete cleft lip and palate. *Cleft Palate Craniofac J* 2009;46:154–160
21. Huang H, Li Y, Luo X, et al. Mechanical analyses of critical surgical maneuvers in the correction of cleft lip nasal deformity. *PLoS One* 2018;13:e0195583
22. Luo X, Yang B, Sheng L, et al. CAD based design sensitivity analysis and shape optimization of scaffolds for bio-root regeneration in swine. *Biomaterials* 2015;57:59–72
23. von Mises R. Mechanik der festen Körper im plastisch-deformablen Zustand: Nachrichten von der Gesellschaft der Wissenschaften zu Göttingen. *Mathematisch-Physikalische Klasse* 1913;1913:582–592
24. Fisher DM, Mann RJ. A model for the cleft lip nasal deformity. *Plast Reconstr Surg* 1998;101:1448–1456
25. Lee SJ, Liong K, Tse KM, et al. Biomechanics of the deformity of septal L-Struts. *Laryngoscope* 2010;120:1508–1515
26. Liong K, Lee SJ, Lee HP. Preliminary deformational studies on a finite element model of the nasal septum reveals key areas for septal realignment and reconstruction. *J Med Eng* 2013;2013: 250274
27. Lee SJ, Liong K, Lee HP. Deformation of nasal septum during nasal trauma. *Laryngoscope* 2010;120:1931–1939
28. Mau T, Mau ST, Kim DW. Cadaveric and engineering analysis of the septal L-strut. *Laryngoscope* 2007;117:1902–1906
29. Oliaei S, Manuel C, Protsenko D, et al. Mechanical analysis of the effects of cephalic trim on lower lateral cartilage stability. *Arch Facial Plast Surg* 2012;14:27–30
30. Jung JW, Park JH, Hong JM, et al. Octahedron pore architecture to enhance flexibility of nasal implant-shaped scaffold for rhinoplasty. *Int J Precis Eng Manuf* 2014;15:2611–2616
31. Wexler D, Segal R, Kimbell J. Aerodynamic effects of inferior turbinate reduction: computational fluid dynamics simulation. *Arch Otolaryngol Head Neck Surg* 2005;131:1102–1107
32. Kimbell JS, Frank DO, Laud P, et al. Changes in nasal airflow and heat transfer correlate with symptom improvement after surgery for nasal obstruction. *J Biomech* 2013;46:2634–2643
33. Shadfar S, Shockley WW, Fleischman GM, et al. Characterization of postoperative changes in nasal airflow using a cadaveric computational fluid dynamics model: supporting the internal nasal valve. *JAMA Facial Plast Surg* 2014;16:319–327
34. Cannon DE, Frank DO, Kimbell JS, et al. Modeling nasal physiology changes due to septal perforations. *Otolaryngol Head Neck Surg* 2013;148:513–518
35. Rhee JS, Cannon DE, Frank DO, et al. Role of virtual surgery in preoperative planning: assessing the individual components of functional nasal airway surgery. *Arch Facial Plast Surg* 2012;14: 354–359
36. Rhee JS, Pawar SS, Garcia GJ, et al. Toward personalized nasal surgery using computational fluid dynamics. *Arch Facial Plast Surg* 2011;13:305–310
37. Nolst Trenité GJ. *Rhinoplasty: A Practical Guide to Functional and Aesthetic Surgery of the Nose*. Amsterdam; New York: Kugler Publications; 1993:x, 200 pp